ISSN: 2710-0723

Research on Measurement and Prediction of Well Blowout Fluid Flow Rate based on Machine Vision

Haimin Cai, He Zhang

School of Mechanical and Electrical Engineering, Southwest Petroleum University, Chengdu 610500, China

Abstract

A machine vision-based method for measuring and predicting well blowout fluid flow rate is proposed to solve the problems of limited quantitative identification of well blowout fluid flow rate, inability to install traditional measurement equipment in the field, and inability to accurately measure and predict blowout fluid flow rate. This method establishes an image processing model based on ORB-BF-RANSAC for blowout sequence images, feature extraction and feature identification are performed on the blowout images from consecutive frames in order to obtain the coordinates of the feature points within the well blowout images. The pixel displacement of the feature point pairs is then calculated. Subsequently, the true displacement of the feature points is calculated using the pinhole imaging principle. Finally, the true displacement is divided by the number of frames to calculate the blowout fluid flow rate. Compared to the speed of mass flow meter calibration, the method achieves a measurement accuracy of 91%. Based on the above method, a well blowout fluid flow rate prediction method is designed by introducing Spatial Attention Mechanism (SAM) to improve the Graph Convolutional Networks (GCN). The prediction model proposed in this paper is more effective compared with other prediction methods, and the Root Mean Square Error (RMSE), Mean Absolute Error (MAE), and Mean Absolute Percentage Error (MAPE) are 12.39%, 18.72% and 9.16%.

Keywords

Machine Vision; Flow Rate Measurement; Image Processing; Feature Recognition; Drilling Blowout.

1. Introduction

As a major source of energy for the country, oil and gas are vital to national economy and the people's livelihood, but the exploitation of oil and gas resources is accompanied by a variety of accidents, the most dangerous of which is the blowout accident [1]. When a well blowout occurs, it will make the environment hot and high-pressure, and the violent and harmful nature of the blowout accident makes it impossible for rescue and relief personnel to take rapid and effective measures to control the accident at close range[2], leading to its intensification and the spewing of harmful substances from the strata, posing a threat to human health, a burden to the environment and a fatal blow to flora and fauna[3-5]. On 20 April 2010, a blowout occurred at the Macondo oil well in the Gulf of Mexico, killing 11 crew members. The blowout was not fully brought under control until 10 July. The accident ultimately resulted in the spill of 4 million barrels of crude oil and at least 2500 square kilometers of seawater covered in oil [4,5].

Accurate measurement of blowout fluid flow rates is required during the rescue process of a blowout accident to provide data to support the development of a reasonable emergency response plan. However, due to the high temperature and high noise environment of the well blowout site, making the current measurement means of safety hazards, problems found

ISSN: 2710-0723

lagging[6], especially the limited ability to quantify the identification of the well blowout fluid flow rate, the traditional measurement means of error, the equipment can not be installed on site, the well blowout flow rate prediction can not be accurately carried out, safety prevention and control measures can not be accurately controlled in a timely manner, resulting in the emergency command strategy is not timely, and thus causing malignant accidents.

Machine vision technology is currently used in various fields, for example, to achieve target detection using smart cameras[7]; to assist in rescue operations using firefighting robots[8];and to detect skin conditions using related medical systems[9].Machine vision technology is mostly aimed at objects with obvious contour shapes, while the target of this paper is a liquid well jet object, whose contour shape is difficult to maintain a fixed shape, making it difficult to obtain well jet parameters by traditional methods.

In conclusion, the study of the blowout fluid flow rates is still at the stage of theoretical derivation and numerical simulation. This paper makes the following contributions to the problem that the measurement of well blowout fluid flow rates fails to be real time and fast, and that existing instruments must be used by personnel to measure parameters in depth at high-temperature and high-pressure accident sites, which does not protect the lives of those working on site.

Firstly, we propose a sequence image processing model based on ORB-BF-RANSAC and a well blowout fluid flow velocity measurement method based on pinhole imaging principles, which enables rapid measurement of blowout fluid flow rate in the early stages of a blowout accident without the need for personnel to measure the parameters at close range in a complex accident site. Secondly, it is not enough just to measure the blowout fluid flow rate in real time, but we also propose a blowout fluid flow rate prediction method based on Spatial Attention-based Graph Convolutional Networks - Long Short-Term Memory Networks (SAGCN-LSTM), which can predict the flow rate changes in advance and help the commanders to make the command and decision.

2. Related Works

Kikani's ultra-short transient rate calculations using a finite element pipeline model for sulfur-bearing gas wells in the South Oldenburg region of Germany [10]. P. Oudeman estimated the blowout rate at different plumes by analyzing the height of the gas-liquid mixed blowout plume [11]. A.R. Hasan's trial-and-error calculations using a transient transport model16 for two-phase flow to achieve estimates of well blowout rates [12]. Liujuan Tang injected crude oil and silicone oil at atmospheric pressure and liquid CO2 into water under simulated deep-sea conditions to obtain quantitative droplet size spectra. It is concluded that with the increase of the jet velocity, the breakup length of the laminar jet increases, and an instability phenomenon leading to sinusoidal fluctuations of the jet and polydispersity of the droplets emerges [13]. Arild proposes a structured probabilistic approach in which the relevant parameters affecting the well blowout rate are analyzed using the BlowFlow tool with a high degree of visualization of the results [14]. E. Hajidavalloo installed flow tubing at the wellhead and varied the size of the tubing to study its effect on the blowout flow rate [15]. A. Turner and P. Loustau use blowout preventers for blowout-related parameter measurements, which are fast and work consistently in complex environments [16]. M. D. Dunn predicted the blowout fluid flow velocity under free-field conditions and concluded that the jet velocity decreases with increasing jet height as the natural entrainment generated by air flows radially into the jet[17].

M. Evestedt and Alexander Medvedev have studied the critical state of a gas jet impacting a liquid surface based on machine vision techniques, using a high-speed camera to acquire multiple frames of the critical state of the gas-liquid collision and analyzing it by using image contour extraction techniques [18]. J. D. Osorio-Cano acquires high-flow hydrological videos in

ISSN: 2710-0723

a laboratory setting and calculates the velocity and flow of high-speed water streams using image variance (IV) and threshold segmentation with path discretization (TSPD) methods [19]. M. W. da Silva Oliveira conducted an experimental study of image local feature descriptors for the image processing part of machine vision, decomposing the local texture space based on partial derivatives, allowing texture feature extraction at different levels of geometric structure, and validating it with a database and classical image feature descriptors [20]. C. Alcan proposes a visual tracking method based on droplet structure and motion feature detection to explain the potential jet phenomenon [21]. M. Mirzaei investigates fluorescence images of supersonic jets based on image processing methods and verifies the high agreement between image processing methods and numerical simulation methods [22].

3. Methodology

3.1. Well Blowout Sequences Images Processing Model

ORB is an optimized image feature matching model based on the principle of FAST key point detector and BRIEF descriptor. FAST can efficiently perform feature point detection, but it lacks directionality, so ORB model introduces the principle of simple and effective intensity center of mass angle direction measurement method, so that the key points of ORB have directional components and rotational invariance [23]. A scale pyramid is used and FAST features are generated at each level of the pyramid to ensure the scale invariance of the ORB model [24,25].

The ORB model uses the grayscale center of mass method to determine the main direction of the feature point: first, the grayscale center of mass C in the neighborhood of the feature point is determined, and then the direction vector of the geometric center O of the local region of the feature point pointing to the grayscale center of mass C is constructed. The center of mass C of the image block and the direction θ of the feature point are expressed as:

$$\begin{cases} m_{pq} = \sum_{x,y} x^p y^q I(x,y) \\ C = (\frac{\mathrm{m}_{10}}{\mathrm{m}_{00}}, \frac{\mathrm{m}_{01}}{\mathrm{m}_{00}}) \\ \theta = \arctan(\frac{\mathrm{m}_{01}}{\mathrm{m}_{10}}) \end{cases} \tag{1}$$

where $I(x,y)$ is the gray value at pixel point(x,y), m_{00} denotes the zero moment, and m_{01}, m_{10} denote the first order moment.

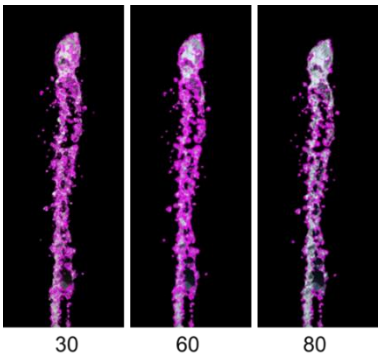

Fig. 1 Effect of ORB for blowout fluid feature points detection under different thresholds

ISSN: 2710-0723

As shown in Fig.1, which demonstrates the effect of ORB for blowout fluid feature points detection under different thresholds, where the thresholds of (a), (b), and (c) are 30, 60, and 80, respectively. From the Fig.1, it can be concluded that when the ORB threshold is 60, the detected overlapping feature points are less, and the corner points and key feature points have been detected, therefore, this paper uses this threshold for the detection of the blowout fluid feature points.

In this paper, feature matching is done by using the BF model, which calculates binary feature descriptors by Hamming distance to complete the similarity calculation between feature points. The Hamming distance calculates the similarity of binary feature vectors by bitwise dissimilarity operation and the result is bit-counted to achieve feature matching. The Hamming distance reflects the similarity of two strings of equal length by calculating the number of different characters at the corresponding positions, and the Hamming distance metric is expressed as:

$$d = \sum_{i=1}^{n} x[i] \oplus y[i] \tag{2}$$

where$x[i]$,$y[i]$is the i-th string of the two feature descriptors; $\oplus$is the iso-or operator.

RANSAC is a robust iterative estimation model that can compute a reasonable set of model parameters in the presence of outliers in the dataset [26], and this paper uses the RANSAC model to filter out the feature points that are mis-matched by the ORB-BF model. RANSAC assumes that the data contains correct data and abnormal data, with correct data recorded as inliers and abnormal data recorded as outliers, and the steps are as follows:

1) Randomly sample K points in the sample.

2) Fit the model to these K points.

3) Calculate the distance from other points to the fitted model and set the threshold, if it is greater than the threshold, it is outliers and discarded, if it is less than the threshold, it is inliers and count the number of inliers.

4) Then, with the new inliers as the basis, carry out step 2 again to get the new fitted model, iterate M times, and select the model with the highest number of inliers, which is the optimal model.

3.2. Method of Calculating the Flow Rate

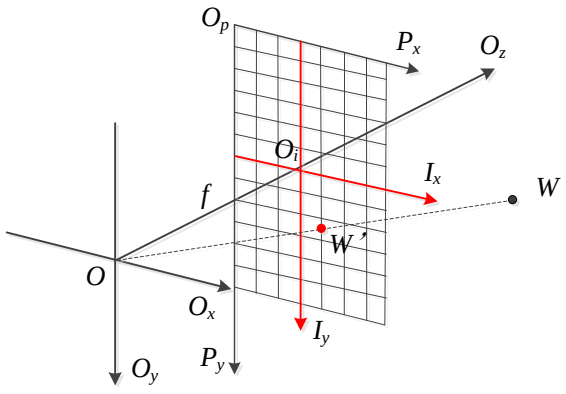

Fig. 2 The principle diagram of pinhole imaging

When using pinhole imaging to calculate the flow rate of blowout fluid, the calibration of the camera is required to determine the internal and external parameters of the camera [27,28].

ISSN: 2710-0723

The outer parameters need to be converted from the pixel coordinate system to the world coordinate system to complete the calculation of blowout fluid flow rate[29], the principle of pinhole imaging is shown in the Fig.2.

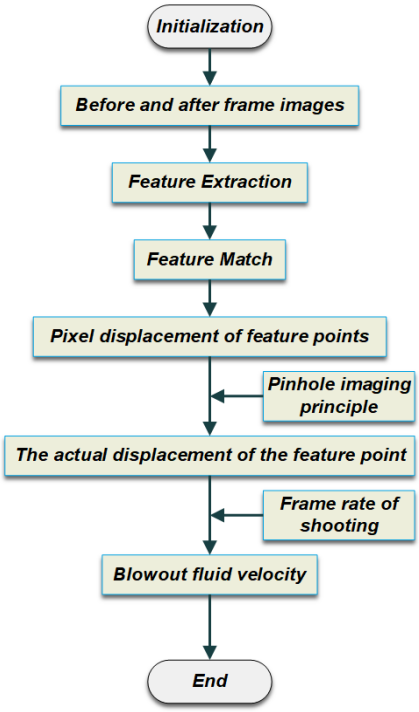

Fig. 3 Flow chart of blowout fluid flow rate calculation

In this paper, the calculation of flow rate is based on the images of adjacent frames, and feature extraction and feature matching are performed on the images to calculate the displacement of the feature points of adjacent frames, which is combined with the acquisition frame rate for flow rate calculation. The flow rate calculation process of the blowout fluid is shown in Fig.3. The blowout fluid flow rate is expressed as:

$$v = \frac{F\sqrt{\left(\Delta mDdx\right)^2 + \left(\Delta nDdy\right)^2}}{f} \tag{3}$$

Where f is the focal length of the high-speed camera,D is the distance of the high-speed camera from the blowout fluid, F is the acquisition frame rate of the high-speed camera, $dx \times dy$ is the pixel size of the sensor in the high-speed camera, and $(\Delta m, \Delta n)$ is the pixel displacement of the feature points in the imaging plane of the adjacent frames.

3.3. Improved GCN

GCN is used to extract spatial correlation features. For the problem of huge experimental parameters and high model complexity in blowout fluid flow rate measurement, SAGCN introduce SAM to improve the GCN to adjust the importance of different nodes.

There is a correlation between the feature points of the injection fluid, and the correlation between the feature points at different locations is very dynamic. The injection velocities of neighboring feature points are likely to affect each other, but the injection velocities of feature points that are far away from each other do not have much effect on each other. Therefore, the input feature matrix X can be processed by using SAM, which is an adaptive approach to

ISSN: 2710-0723

dynamically capture the correlation of each feature point in the spatial dimension[30,31], and weights can be assigned to each injection fluid feature point to better capture the relationships and dynamics between feature points.

The spatial attention mechanism assigns different weights to each feature point, and the spatial attention matrix is expressed as:

$$S_{i,j} = V_S \cdot \sigma\left\{\left(X \cdot W_1\right) \cdot W_2 \cdot \left(W_3 \cdot X\right)^T + b_s\right\} \tag{4}$$

$S_{i,j} \in \mathbb{R}^{N \times N}$ is dynamically computed from the input X of the current network by the attention scoring function, and the result is the distribution of each feature point in the blowout sequence image. $X \in \mathbb{R}^{N \times C \times T}$ is the input to the spatial attention module, N represents the N nodes on the topology, and T represents T time steps.$W_1 \in \mathbb{R}^T$,$W_2 \in \mathbb{R}^{T \times C}$,$W_3 \in \mathbb{R}^C$ are the weight matrices, $V_S \in \mathbb{R}^{N \times N}$are the coefficients of the σ function, $b_S \in \mathbb{R}^{N \times N}$is the bias function, and σ is $sigmoid$ function, being used as the activation function.

The spatial attention mechanism assigns different weights to each feature point, and the spatial attention matrix is expressed as:

$$S_{i,j} = V_S \cdot \sigma\left\{\left(X \cdot W_1\right) \cdot W_2 \cdot \left(W_3 \cdot X\right)^T + b_s\right\} \tag{5}$$

$S_{i,j} \in \mathbb{R}^{N \times N}$ is dynamically computed from the input X of the current network by the attention scoring function, and the result is the distribution of each feature point in the blowout sequence image. $X \in \mathbb{R}^{N \times C \times T}$ is the input to the spatial attention module, N represents the N nodes on the topology, and T represents T time steps.$W_1 \in \mathbb{R}^T$,$W_2 \in \mathbb{R}^{T \times C}$,$W_3 \in \mathbb{R}^C$ are the weight matrices, $V_S \in \mathbb{R}^{N \times N}$are the coefficients of the σ function, $b_S \in \mathbb{R}^{N \times N}$is the bias function, and σ is $sigmoid$ function, being used as the activation function.

The probability distribution vector is represented by the attention distribution $\alpha_{i,j}$, and the spatial attention matrix $S_{i,j}$ is normalized by the $SoftMax$ function, and they are expressed as follows:

$$\alpha_{i,j} = \frac{e^{s_{i,j}}}{\sum_{j=1}^{N} e^{s_{i,j}}} \tag{6}$$

$\alpha_{i,j}$ is the weight distribution of each feature point in the well sequence image, and Fig.4 illustrates the calculation process of the spatial attention mechanism. The feature information of different nodes is brought together to form a spatial feature matrix, it can be expressed as:

$$\hat{A} = A\alpha_{i,j} \tag{7}$$

ISSN: 2710-0723

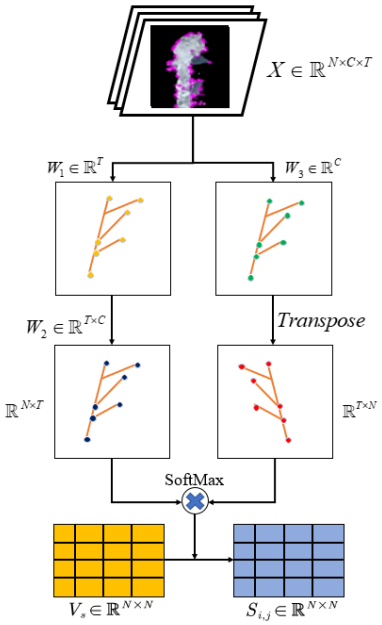

Fig. 4 Calculation process of spatial attention mechanism

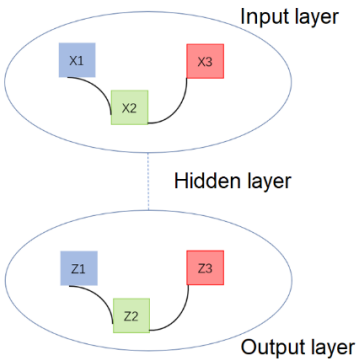

Fig. 5 GCN feature transformation

We use a two-layer GCN to obtain the spatial correlation of the blowout fluid, with the activation function $ReLU$, The output $\hat{A}$ and the feature matrix X processed by the spatial attention mechanism are input into the GCN for feature transformation, and the process is shown in Fig.5, and the output is:

$$Z = f(X, A)SoftMax\left(\tilde{A}ReLU(\tilde{A}XW^{(0)})W^{(1)}\right) \tag{8}$$

Where $W^{(0)}$ and $W^{(1)}$ denote the weight matrices of the first two layers of the convolutional network, respectively, $ReLU$ is the rectified linear unit, and $SoftMax$ is the normalization function.

3.4. LSTM

We rely on the LSTM to extract the temporal relationships of the images of the blowout sequence, and process the output Z of the SAGCN.A set of independent two-layer LSTM networks was constructed to analyze the temporal correlation of the blowout fluid on the basis of SAGCN, so as to obtain the spatio-temporal correlation characteristics of the blowout flow. It can be expressed as follows:

ISSN: 2710-0723

$$\begin{cases} H_k^{(2)} = LSTM_k^{(2)}\left(H_k^{(l)}\right) \\ H_k^{(l)} = LSTM_k^{(l)}\left(G^{(2)}\right) \end{cases} \tag{9}$$

where $H_k^{(2)}$ denotes the output of the feature vector of the kth channel in $G^{(2)}$ after two layers of LSTM network. The structure of the two-layer LSTM network is the same, and $LSTM_k^{(l)}$ is used as an example for illustration, and the hidden state of $LSTM_k^{(l)}$ at the ith time step is expressed as follows:

$$\begin{cases} F_{i,k} = \sigma\left(W_{FH,k}H_{i-1,k}^{(l)} + W_{Fx,k}G_{i,k}^{(2)} + b_{F,k}\right) \\ I_{i,k} = \sigma\left(W_{IH,k}H_{i-1,k}^{(l)} + W_{Ix,k}G_{i,k}^{(2)} + b_{I,k}\right) \\ \tilde{C}_{i,k} = \tanh\left(W_{CH,k}H_{i-1,k}^{(l)} + W_{Cx,k}G_{i,k}^{(2)} + b_{C,k}\right) \\ C_{i,k} = F_{i,k}\cdot C_{i-1,k} + I_{i,k}\cdot\tilde{C}_{i,k} \\ O_{i,k} = \sigma\left(W_{OH,k}H_{i-1,k}^{(l)} + W_{Ox,k}G_{i,k}^{(2)} + b_{O,k}\right) \\ H_{i,k}^{(1)} = O_{i,k}\cdot\tanh\left(C_{i,k}\right) \end{cases} \tag{10}$$

where $W_{FH,k}$, $W_{IH,k}$, $W_{CH,k}$, $W_{OH,k}$, $W_{Fx,k}$, $W_{Ix,k}$, $W_{Cx,k}$ are the weight parameter matrices,$b_{F,x}$,$b_{I,x}$,$b_{C,k}$,$b_{O,k}$ are the bias vectors. The final output $H_k^{(2)}$ is obtained from the two-layer LSTM structure of all channels together, where the $H_k^{(2)}$ obtained for each channel characterizes the spatio-temporal correlation of the blowout fluid in terms of the dimensionality of that channel.

4. Experiments and Analysis

4.1. Design of the Image Acquisition Scheme

To validate the performance of the proposed ORB-BF-RANSAC image processing model and to acquire data sets for the SAGCN-LSTM prediction model, simulated blowout experiments were conducted.

The video acquisition frame rate was set to 480 FPS, and video acquisition under background optimization and natural background was performed by controlling the focal length f of the camera, the distance d between the camera and the nozzle, and the camera height H kept constant. Video acquisition and flow rate calculation are performed in parallel to complete real-time flow rate calculation and prediction. The experimental site is shown in Fig.6, and the acquisition scheme and parameter settings are shown in Table 1.

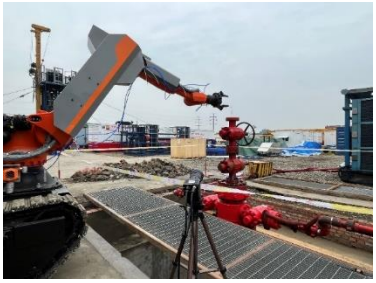

Fig. 6 Experimental site

ISSN: 2710-0723

Table 1. Setting of video acquisition parameters

Frame rate of acquisition:480FPS	
d =240cm H =150cm	Speed sequence 1
	Speed sequence 2
	Speed sequence 3
	Speed sequence 4
	Speed sequence 5
	Speed sequence 6
	Speed sequence 7
	Speed sequence 8
	Speed sequence 9
	Speed sequence 10
	Speed sequence 11
	Speed sequence 12

In the process of blowout video acquisition, control the shooting background constant, focal length constant, change the valve opening of the shut-off valve, shoot video at different flow rates, and record the fluid flow rate measured by the mass flow meter on the upper computer. As shown in Fig.7, the video acquisition process for the simulated blowout fluid experiment:

(1) Centrifugal pumps as the drive source;

(2) Mass flow meter to calibrate the flow rate;

(3) flow control by using a shut-off valve;

(4) Rigid components are installed at the nozzle to scale the orifice diameter to simulate the blowout jet.

4.2. Analysis of Flow Rate Measurement Results

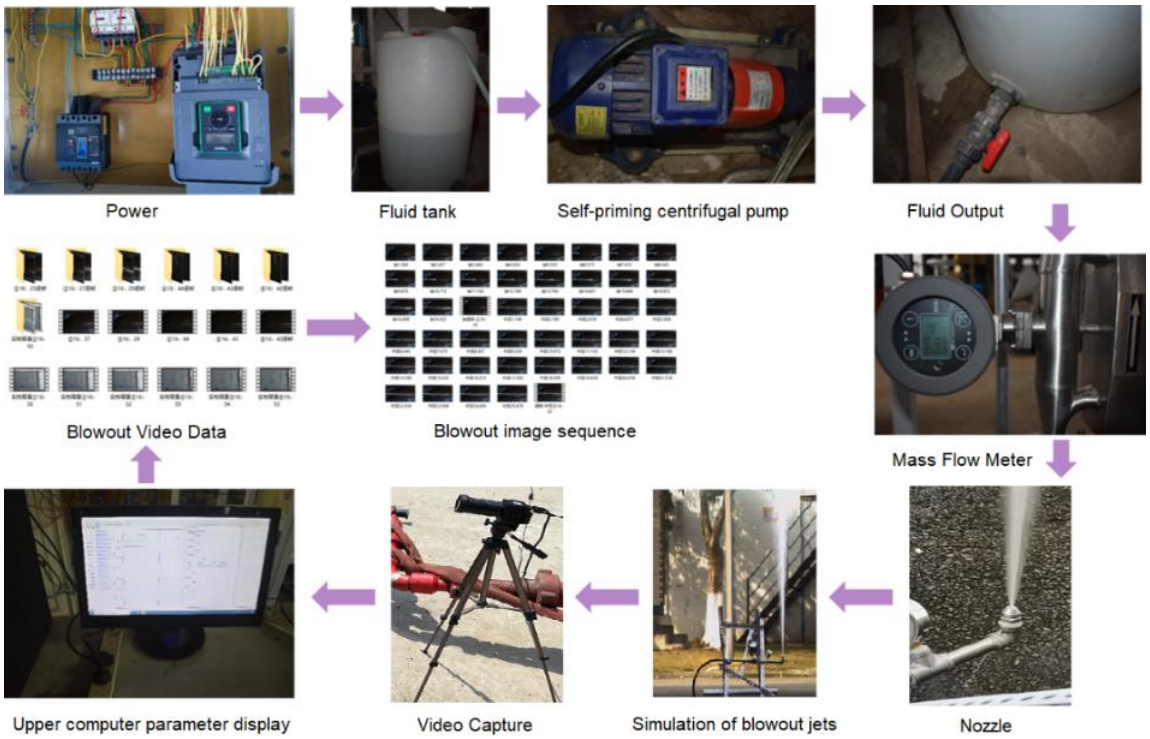

Fig. 7 The video acquisition flow of the simulated blowout fluid experiment

ISSN: 2710-0723

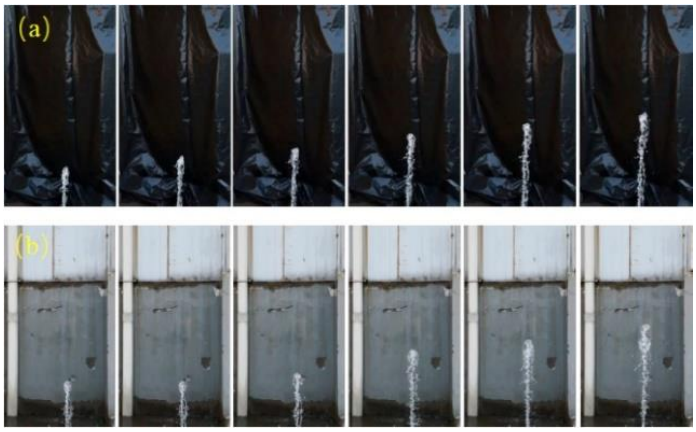

Fig. 8 Sequence images

The video is processed into an image sequence as shown in Fig.8. The background of (a) is the optimized background, and the background of (b) is the natural background. The ORB-BF-RANSAC image processing model is then used to extract the feature points of the fluid from the image sequence and perform feature matching, and then calculate the pixel displacement of the feature points. Based on the pinhole imaging principle, the real-world displacements are calculated, and finally the blowout fluid flow rate is calculated based on the acquisition frame rate.

The feature point extraction of the well blowout sequence image is shown in Fig.9. The feature matching results of ORB-BF and ORB-BF-RANSAC are shown in Fig.10. After using the RANSAC to reject the mis-matched pairs of blowout images, the number of mis-matched lines in the figure is significantly reduced and the feature points of two adjacent frames of blowout images are better matched.

The blowout fluid adjacent frame matching map obtained with the model is displayed in the form of pixel point coordinates, as shown in Fig.11. The calculated fluid flow rate of the blowout was compared with the velocity calibrated by the mass flow meter, as shown in Fig.12 and Table 2. It can be seen from Table 2 that the calculated velocity is relatively accurate, with a maximum relative error of 8.52%. When the flow rate exceeds 120 m/s, the measurement accuracy is still higher than 91%, which is a good way to achieve the measurement of the flow rate of the well blowout fluid.

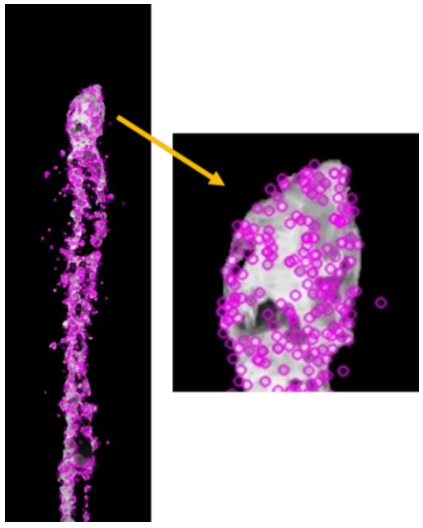

Fig. 9 Feature point extraction of ORB

ISSN: 2710-0723

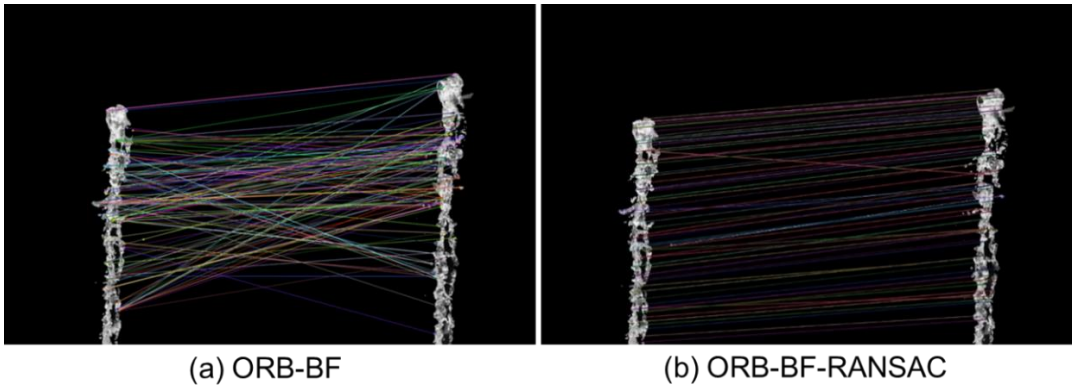

Fig. 10 The feature matching results

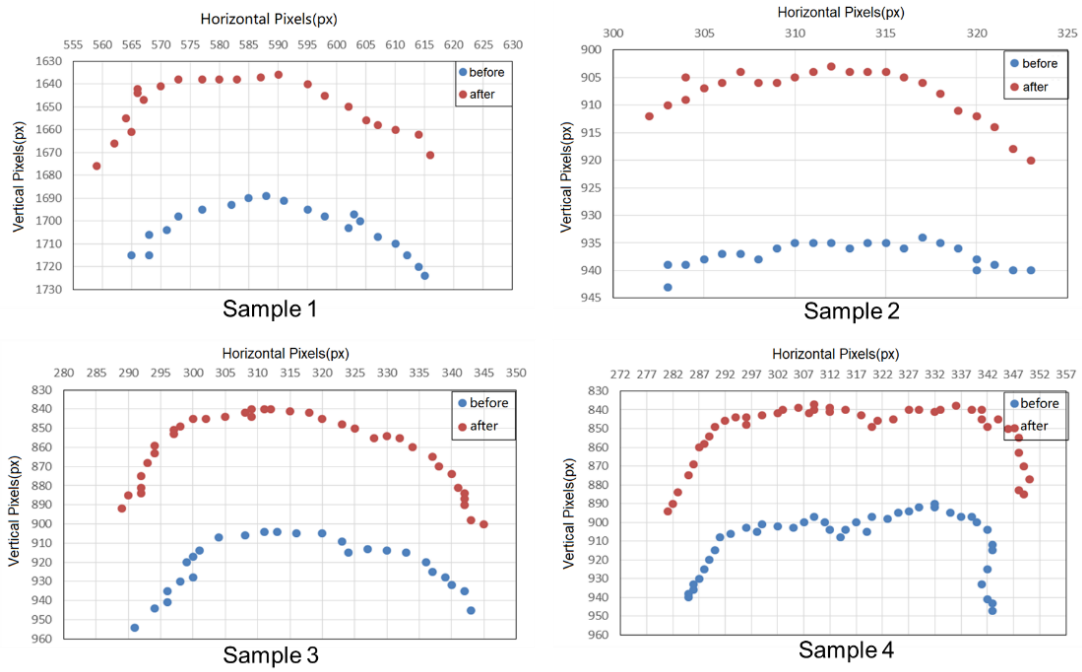

Fig. 11 Pixel distribution of feature points

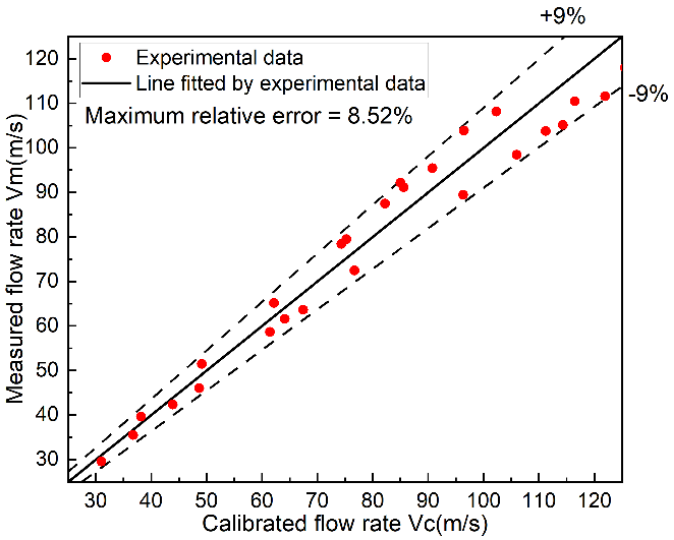

Fig. 12 Comparison of measured flow rate and calibrated flow rate

ISSN: 2710-0723

Table 2. Results of measured flow rate compared to calibrated flow rate

Samples	Measured flow rate V_m(m/s)	Calibrated flow rate V_c(m/s)	Accuracy(%)
1	11.462	11.076	96.51%
2	29.561	31.026	95.28%
3	46.042	48.667	94.61%
4	63.633	67.476	94.30%
5	79.473	75.236	94.37%
6	87.432	82.227	93.67%
7	91.114	85.616	93.58%
8	103.853	96.492	92.37%
9	110.886	120.980	91.66%
10	133.062	122.615	91.48%

4.3. Datasets and Evaluation Metrics of Prediction

After a blowout accident, it is not enough to measure the flow rate of the blowout in real time, but to predict the flow rate in advance can better help the field staff to command the emergency operations on site. Therefore, in this paper, the flow rate prediction is studied to help the field personnel to better judge the situation and make scientific decisions.

The flow rates measured by the above experiments are made into a data set Blowout. To evaluate the effectiveness of the models, they are compared with seven prediction models, which include HA, ARIMA, SVR, GRU. We also compare the prediction results of the unoptimized GCN-LSTM and the Mean Absolute Error (MAE), Root Mean Square Error (RMSE), and Mean Absolute Percentage Error (MAPE) of each model are calculated as evaluation metrics and conduct a comparative analysis to achieve an objective evaluation of the model performance, they can be expressed as:

$$\begin{cases} MAE = \frac{1}{n}\sum_{1}^{n}\left|y_p - y_r\right| \\ RMSE = \sqrt{\frac{1}{n}\sum_{i=1}^{n}(y_p - y_r)^2} \\ MAPE = 100\% \times \frac{1}{n}\sum_{1}^{n}\left|\frac{y_p - y_r}{y_r}\right| \end{cases} \tag{11}$$

where y_p is the predicted data and y_r is the actual data.

4.4. Prediction Result Evaluation

As shown in Table 3, the SAGCN-LSTM proposed in this paper outperforms the other models on the Blowout dataset and improves in each evaluation metric compared to the other methods. Since both HA and ARIMA are linear models that only consider information in the time dimension, their prediction performance is relatively poor. SVR and GRU use machine learning methods to analyze the data and have better nonlinear mapping capabilities than HA and ARIMA, but only analyze the data in the time dimension without considering the spatial dimension, so their prediction performance is only better than HA and ARIMA.

The SAGCN-LSTM introduces SAM, which considers the information of temporal and spatial dimensions, so the SAGCN-LSTM achieves better prediction results than the GCN-LSTM. the accuracy of the SAGCN-LSTM compared with the GCN-LSTM in the evaluation metrics RMSE, MAE and MAPE is improved by 12.39%, 18.72% and 9.16%.

ISSN: 2710-0723

Table 3. Performance comparison of models

Models	Blowout		
	RMSE(%)	MAE(%)	MAPE(%)
HA	52.61	36.46	19.49
ARIMA	65.43	31.88	18.87
SVR	43.57	28.54	16.73
GRU	42.37	27.87	16.07
GCN-LSTM	35.43	22.17	14.52
SAGCN-LSTM	31.04	18.02	13.19

As the prediction interval increases, the prediction error will gradually increase and the prediction effect will inevitably deteriorate, while the SAGCN-LSTM constructed in this paper has less variation in prediction error and outperforms the unoptimized GCN-LSTM.

5. Conclusion

In oil drilling engineering, the realization of long-distance measurement technology of blowout fluid flow rate can help the emergency rescue of early blowout accidents. A ORB-BF-RANSAC-based image processing model for well blowout sequences is proposed, and the flow rate calculation method achieves 91% accuracy in the experiment, which has the value of promotion. Based on the flow rate measurement, the prediction method of well blowout fluid flow rate based on SAGCN-LSTM is proposed, and the RMSE, MAE, and MAPE are 12.39%, 18.72% and 9.16%, with satisfactory prediction effect, which can provide theoretical basis for the decision of command and decision makers at the site of blowout emergency.

Acknowledgments

This work was supported by the Science and Technology Department Project of Sichuan Province, China (2022YFG0243).

References

[1] P. Blotto, M. Bonuccelli, G. Morale, E. Dellarole, M. Falcitelli, F. Podenzani, Development of a Integrated Approach to the Risk Analysis of a Blow-out Accident, SPE International Conference on Health, Safety, and Environment in Oil and Gas Exploration and Production, 2004.

[2] S. Rassenfoss, Report Recounts the Missed Signals Leading to a Blowout That Killed Five, (JPT Emerging Technology Senior Editor) View rights & permissions Vol.71(No.8) (2019) 40-42. https://doi.org/10.2118/0819-0040-jpt.

[3] W.F. Jr., Deepwater Blowout, A Case History; Shallow Gas Hazards Hide-in-the-Weeds, 2007.

[4] T.J. Crone, M. Tolstoy, Magnitude of the 2010 Gulf of Mexico Oil Leak, Lamont-Doherty Earth Observatory, Columbia University, Palisades, NY 10964, USA Department of Earth and Environmental Sciences, Columbia University, Palisades, NY 10964, USA Vol.330(No.6004) (2010) 634. https://doi.org/10.1126/science.1195840.

[5] C.B. Paris, M.L. Hénaff, Z.M. Aman, A. Subramaniam, J. Helgers, D.-P. Wang, V.H. Kourafalou, A. Srinivasan, Evolution of the Macondo Well Blowout: Simulating the Effects of the Circulation and Synthetic Dispersants on the Subsea Oil Transport, University of Miami, Rosenstiel School of Marine and Atmospheric Science, 4600 Rickenbacker Causeway, Miami, Florida 33149-1098, United States;University of Miami, Cooperative Institute for Marine and Atmospheric Studi Vol.46(No.24) (2012) 13293-13302. https://doi.org/10.1021/es303197h.

[6] G.E.E. Jerry Westerweel, R.J. Adrian, Particle Image Velocimetry for Complex and Turbulent Flows, Annual Review of Fluid Mechanics Vol.45(No.1) (2013) 409-436.

ISSN: 2710-0723

[7] A. Hitelman, Y. Edan, A. Godo, R. Berenstein, J. Lepar, I. Halachmi, Biometric identification of sheep via a machine-vision system, Precision Livestock Farming (PLF) Lab., Agricultural Engineering Institute, Agricultural Research Organization (A.R.O.) - Volcani Institute, 68 Hamaccabim Road, P.O.B 15159, Rishon Lezion 7505101, Israel Dept. of I Vol.194 (2022) 106713. https://doi.org/10.1016/j.compag.2022.106713.

[8] A. Dhiman, N. Shah, P. Adhikari, S. Kumbhar, I.S. Dhanjal, N. Mehendale, Firefighting robot with deep learning and machine vision, K. J. Somaiya College of Engineering, Mumbai, India K. J. Somaiya College of Engineering, Mumbai, India K. J. Somaiya College of Engineering, Mumbai, India K. J. Somaiya College of Engineering, Mumbai, India K. J. Somai Vol.34(No.4) (2022) 2831-2839. https://doi.org/10.1007/s00521-021-06537-y.

[9] D. Ribli, A. Horváth, Z. Unger, P. Pollner, I. Csabai, Detecting and classifying lesions in mammograms with Deep Learning, Department of Physics of Complex Systems, Eötvös Loránd University, Budapest, Hungary;3rd Department of Internal Medicine, Semmelweis University, Budapest, Hungary;Department of Radiology, Semmelweis University, Budapest, Hungary;MTA Vol.8(No.1) (2018) 1-7. https://doi.org/10.1038/s41598-018-22437-z.

[10] J. Kikani, A Method for Blowout-Rate Prediction for Sour-Gas Wells, Oldenburg Fields, Germany, (Shell E&P Technology Company);(BEB Erdgas & Erdol Gmbh);(BEB Erdgas & Erdol Gmbh) Vol.11(No.3) (1996) 158-162. https://doi.org/10.2118/35582-pa.

[11] P. Oudeman, Analysis of Surface and Wellbore Hydraulics Provides Key to Efficient Blowout Control, (Shell Intl. E&P) Vol.13(No.3) (1998) 163-173. https://doi.org/10.2118/51179-pa.

[12] A.R. Hasan, C.S. Kabir, D. Lin, Modeling Wellbore Dynamics During Oil Well Blowout, International Oil and Gas Conference and Exhibition in China, 2000.

[13] L. Tang, S.M. Masutani, Laminar to Turbulent Flow Liquid-liquid Jet Instability And Breakup, The Thirteenth International Offshore and Polar Engineering Conference, 2003.

[14] Ø. Arild, K.K. Fjelde, A. Merlo, B. Daireaux, T. Løberg, BlowFlow - a New Tool within Blowout Risk Management, IADC/SPE Asia Pacific Drilling Technology Conference and Exhibition, 2008.

[15] E. Hajidavalloo, P. Omidian, Modeling and Simulation of Flow Field Around a Blowout Well, SPE Journal Vol.17(No.1) (2012) 212-218. https://doi.org/10.2118/149777-pa.

[16] A. Turner, P. Loustau, Fiber Optic Sensor Based Monitoring System for Blowout Preventer, Offshore Technology Conference, 2015.

[17] M.D. Dunn, S. Fitzgerald, J.B. Garner, Predicting Hydrocarbon Burn Efficiency of Ignited Blowout for Oil Spill Source Control, IADC/SPE Drilling Conference and Exhibition, 2018.

[18] M. Evestedt, A. Medvedev, GAS JET IMPINGING ON LIQUID SURFACE: CAVITY SHAPE MODELLING AND VIDEO-BASED ESTIMATION, Department of Information Technology, Uppsala University, P. O. Box 337, SE-951 05, SWEDEN Vol.38(No.1) (2005) 1065-1070. https://doi.org/10.3182/ 200507 03-6-cz-1902.00178.

[19] J.D. Osorio-Cano, A. Osorio, eacute, s. F, R. Medina, A method for extracting surface flow velocities and discharge volumes from video images in laboratory, Research group OCEANICOS, Department of Geosciences and Environment, Universidad Nacional de Colombia sede Medellín, Carrera 80 #65-223, Medellín, Colombia; Instituto de Hidráulica Ambiental (IH), Universidad de Canta Vol.33 (2013) 188-196. https://doi.org/10.1016/j.flowmeasinst.2013.07.009.

[20] M.W.d.S. Oliveira, N.R. da Silva, A. Manzanera, O.M. Bruno, Feature extraction on local jet space for texture classification, [1] Univ Sao Paulo, Inst Math & Comp Sci, USP, BR-13566590 Sao Carlos, SP, Brazil Universidade de Sao Paulo [2] Univ Sao Paulo, Sao Carlos Inst Phys, Sci Comp Grp, BR-13566590 Sao Carlo Vol.439(No.0) (2015) 160-170. https://doi.org/10.1016/j.physa.2015.06.046.

[21] G. Alcan, M. Ghorbani, A. Kosar, M. Unel, A new visual tracking method for the analysis and characterization of jet flow, Mechatronics Engineering Program, Faculty of Engineering and Natural Sciences, Sabanci University Orhanli, Istanbul, Tuzla, Turkey Vol.51 (2016) 55-67. https://doi.org/10.1016/j.flowmeasinst.2016.08.005.

ISSN: 2710-0723

[22] M. Mirzaei, M. Belan, An Application of Image Analysis to Hypersonic Flows, Department of Aerospace Engineering, Politecnico di Milano, Italy Vol.45(No.45) (2013) 01064(1-5). https://doi.org/10.1051/epjconf/20134501064.

[23] P. Chhabra, N.K. Garg, M. Kumar, Content-based image retrieval system using ORB and SIFT features, Department of Computer Science and Engineering, GZS Campus College of Engineering and Technology, Maharaja Ranjit Singh Punjab Technical University, Bathinda, Punjab, India Department of Computational Sciences, Maharaja R Vol.32(No.7) (2020) 2725-2733. https://doi.org/10.1007/s00521-018-3677-9.

[24] X. Wang, J. Zou, D. Shi, An Improved ORB Image Feature Matching Algorithm Based on SURF, 2018 3RD INTERNATIONAL CONFERENCE ON ROBOTICS AND AUTOMATION ENGINEERING (ICRAE) (2018) 218-222.

[25] Z. Zhang, L. Wang, W. Zheng, L. Yin, R. Hu, B. Yang, Endoscope image mosaic based on pyramid ORB, School of Innovation and Entrepreneurship, Xi'an Fanyi University, Xi'an 710105, P.R.China;School of Automation, University of Electronic Science and Technology of China, Chengdu 610054, P.R.China;Department of Vol.71(Part B) (2022) 103261. https://doi.org/10.1016/j.bspc. 2021. 103261.

[26] W. Wu, W. Liu, An optimized method based on ransac for fundamental matrix estimation, 2018.

[27] J.S.B.L.X.-H.W.J.-M. Li, Study of the Parallax Correction Algorithm Based on the Multiple Regulatory Factors, School of Electrical and Information Engineering,Jiangsu University,Zhenjiang,212013, China2012.

[28] M.J. Jia, X. Cao, J.R. Gunn, P. Bruza, S. Jiang, B.W. Pogue, Tomographic Cherenkov-excited luminescence scanned imaging with multiple pinhole beams recovered via back-projection reconstruction, Optics letters Vol.44(No.7) (2019) 1552-1555. https://doi.org/10.1364/ol.44.001552.

[29] Z. Jiang, Y. Kong, W. Qian, S. Wang, C. Liu, Resolution and signal-to-noise ratio enhancement for synthetic coded aperture imaging via varying pinhole array, ; Jiangnan Univ, Computat Opt Lab, Dept Optoelect Informat Sci & Technol, Sch Sci, Wuxi 214122, Jiangsu, Peoples R China Jiangnan University ; Chinese Acad Sci, Shanghai Inst Opt & Fine Mech, Shanghai 201800, Peoples R China Vol.58(No.22) (2019) 6157-6164. https://doi.org/10.1364/ao.58.006157.

[30] Z. Niu, G. Zhong, H. Yu, A review on the attention mechanism of deep learning, Department of Computer Science and Technology, Ocean University of China, Qingdao 266100, China;School of Creative Technologies, University of Portsmouth, Portsmouth PO1 2DJ, UK Vol.452 (2021) 48-62. https://doi.org/10.1016/j.neucom.2021.03.091.

[31] M. Zhang, H. Su, J. Wen, Classification of flower image based on attention mechanism and multi-loss attention network, Department of Information Engineering, Information Institute, GUI Zhou University of Finance and Economics, Guiyang, 550025, China Vol.179(No.C) (2021) 307-317. https://doi.org/10.1016/j.comcom.2021.09.001.